Article
Chinese Science Bulletin
Geology
September 2012 Vol.57 No.26: 3469–3481
doi: 10.1007/s11434-012-5228-6

Ductile deformation within Upper Himalaya Crystalline Sequence and geological implications, in Nyalam area, Southern Tibet

LIU XiaoBing[1,2,3*], LIU XiaoHan[1], LELOUP P. H.[2], MAHEO G.[2], PAQUETTE J. L.[4], ZHANG XinGang[3] & ZHOU XueJun[1]

[1] *Key Laboratory of Continental Collision and Plateau Uplift, Institute of Tibetan Plateau Research, Chinese Academy of Sciences, Beijing 100085, China;*
[2] *Laboratoire des sciences de la terre de Lyon, Terre, Planètes, Environement, CNRS UMR 5276, Université Lyon1 – ENS Lyon, Villeurbanne, 69622, France;*
[3] *Graduate University of Chinese Academy of Sciences, Beijing 100049, China;*
[4] *Laboratoire Magmas et Volcans, CNRS UMR 6524, Université Blaise Pascal, Clermont-Ferrand, 63038, France*

Received March 27, 2012; accepted April 24, 2012; published online May 26, 2012

The South Tibet Detachment System (STDS) is a flat normal fault that separates the Upper Himalaya Crystalline Sequence (UHCS) below from the Tethyan Sedimentary Sequence (TSS) above. Timing of deformations related to the STDS is critical to understand the mechanism and evolution of the Himalaya collision zone. The Nyalam detachment (ND) (~86°E) locates in the middle portion of STDS (81°–89°E). Dating of deformed leucocratic dykes that are most probably syntectonic at different depth beneath the ND, allow us to constrain the timing of deformation. (1) Dyke T11N37 located ~3500 m structurally below the ND emplaced at 27.4± 0.2 Ma; (2) Dyke T11N32 located ~1400 m structurally below the ND emplaced at 22.0±0.3 Ma; (3) T11N25 located within the top to the north STD shear zone, ~150 m structurally below the ND, emplaced at 17.1±0.2 Ma. Combining ND footwall cooling history and T11N25 deformation temperature, we indicate a probable onset of top to the north deformation at ~16 Ma at this location. These results show an upward younging of the probable timing of onset of the deformation at different structural distance below the ND. We then propose a new model for deformation migration below the ND with deformation starting by pure shear deformation at depth prior to ~27.5 Ma that migrates upward at a rate of ~ 0.3 mm/a until ~18 Ma when deformation switches to top to the north shearing in the South Tibet Detachment shear zone (STDsz). As deformation on the ND stops at 14–13 Ma this would imply that significant top to the North motion would be limited to less than 5 Ma and would jeopardize the importance of lower channel flow.

Upper Himalaya Crystalline Sequence (UHCS), South Tibet Detachment shear zone (STDsz), Nyalam detachment (ND), monazite-zircon U-Th/Pb dating, deformation migration

Citation: Liu X B, Liu X H, Leloup P H, et al. Ductile deformation within Upper Himalaya Crystalline Sequence and geological implications, in Nyalam area, Southern Tibet. Chin Sci Bull, 2012, 57: 3469–3481, doi: 10.1007/s11434-012-5228-6

Since its discovery the South Tibet Detachment System (STDS) [1] has driven the attention of many scientists as this major normal fault results from the India-Eurasia collision. Normal faulting along the STDS has often been associated with magmatism within the Upper Himalaya Crystalline Sequence (UHCS). This magmatism took place from ~24 to ~12 Ma [2–22], with some evidence for an older magmatic activity since ~36 Ma [6,23,24]. In more detail the age range may result from different interpretations of the age populations within each sample, and of the structural relationships of the dated granite with respect to the deformation (pre, syn or post deformation). Another point is that deformation and magmatism could have migrated with time yielding apparently contradictory results.

Some studies have suggested deformation linked with the STDS could have migrated upwards prior to localize in the

*Corresponding author (email: xiao-bing.liu@hotmail.com)

top to the north South Tibet Detachment (STD) shear zone [14,25]. Because this hypothesis has major bearings not only on the history of the STD shear zone but also on the mechanics of the Himalayan range building and on the mechanics of low angle detachment in general, it deserves to be investigated in more details.

For this purpose we dated deformed leucocratic dykes located at various structural depth below the Nyalam detachment, a portion of the STDS.

1 Geological setting

1.1 The South Tibet Detachment System (STDS)

The South Tibetan Detachment System (STDS), corresponds to a series of north dipping faults that parallel the Himalayan belt for more than 1000 km and that accommodate top to the North/normal motion of the Tethyan sedimentary series (TSS) of South Tibet with respect to the underlying High Himalayan crystalline series also called Himalayan crystalline slab (HCS) (Figure 1) [1,26,27]. Normal motion has occurred on several nearly parallel low dipping structures that are from top to bottom: (1) few brittle normal faults in the TSS, (2) a detachment at the contact between the un-metamorphosed TSS and the underlying metamorphic rocks that will be referred here as the South Tibet Detachment (STD), and (3) a ductile shear zone at the top of the HCS, the STD shear zone (STDsz), where gneisses, marbles, quartzites and mylonitic leucogranites are highly deformed, lineation trending NE or NNE and numerous shear criterion indicate a normal motion [1,14,19,24,26,28–30]. Below/within the STDsz, the upper HCS series (UHCS) are intruded by numerous leucogranitic plutons, dykes and sills. The sills are often strongly flattened in the surrounding foliation but some time undeformed dykes crosscut that foliation. Undeformed granites however never crosscut the STD. These granites have been interpreted as having triggered STDS motion [26], or as a consequence of decompression induced by the STDS motion [31]. In many cases ages of the leucogranites have been taken as reflecting motion along the STD (Godin et al. [32] and references therein). The central portion of STDS (81°–89°E, see Yin [33]), spanning from Gurla Mandata (~81°E) to the Zherger La (89°E) (Figure 1), has been studied in several locations. In this contribution we focus on the Nyalam section.

1.2 Nyalam Detachment (ND) and underlying UHCS series

The Nyalam Detachment (ND) [26], is a part of the STD outcropping about 30 km north of Nyalam town [34] (Figure 1 and 2(a)). Near Ruji village, metasediments and leucogranites of the UHCS are strongly deformed in the STDsz with numerous top to the North (normal) shear criteria [21,26]. In this zone foliation trends N70°, 30°N on average and lineation strikes ~N35° (Figure 2(a) and (c)) as in several other localities along the STDS [3,14,15,24,28,30,35,36]. Further to the East the STD is cut and offset by at least two NNW-SSE trending dextral-normal faults (Figure 2(a)). Near ZhaSongLe village, foliation in the UHCS trends N45° and dips 45° to the North (Figure 2(a)). Such geometry may have resulted from the tilting of the whole STD and UHCS

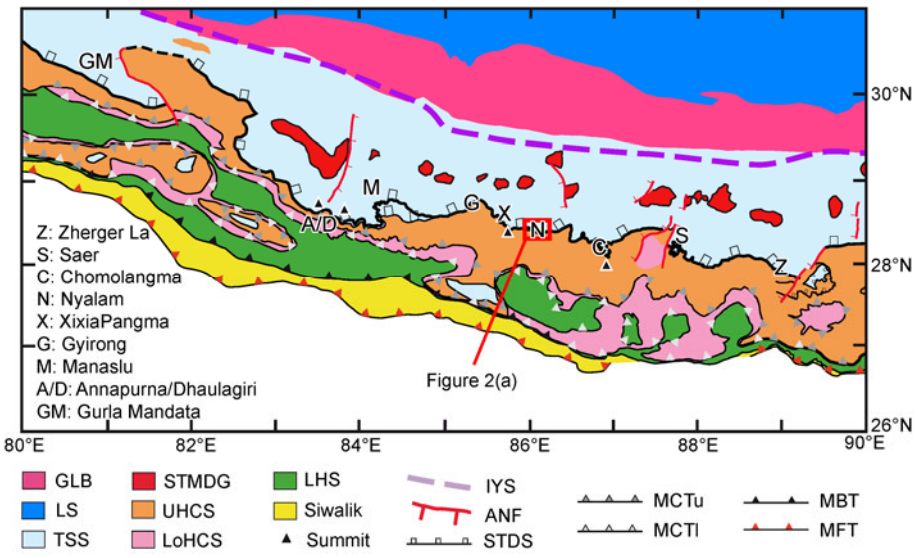

Figure 1 General structural map of the central Himalayan range between 80° and 90°E. Modified from Leloup et al. [14]. GLB, Gangdese and Ladakh batholiths; STMDG, South Tibetan metamorphic domes and granites; TSS, Tethyan Sedimentary Sequence; LS, Lhasa Sequence; UHCS, Upper Himalayan Crystalline Sequence; LoHCS, Lower Himalayan Crystalline Sequence; LHS, Lesser Himalaya Sequence; S, Siwalik; IYS, Indus - Tzangpo Tertiary suture zone; ANF, Active normal faults; STDS, South Tibetan Detachement System; MCTu, upper Main Central Thrust; MCTl, Lower Main Central Thrust; MBT, Main Boundary Thrust; MFT, Main Frontal Thrust. Red rectangular corresponds to the location for Figure 2(a).

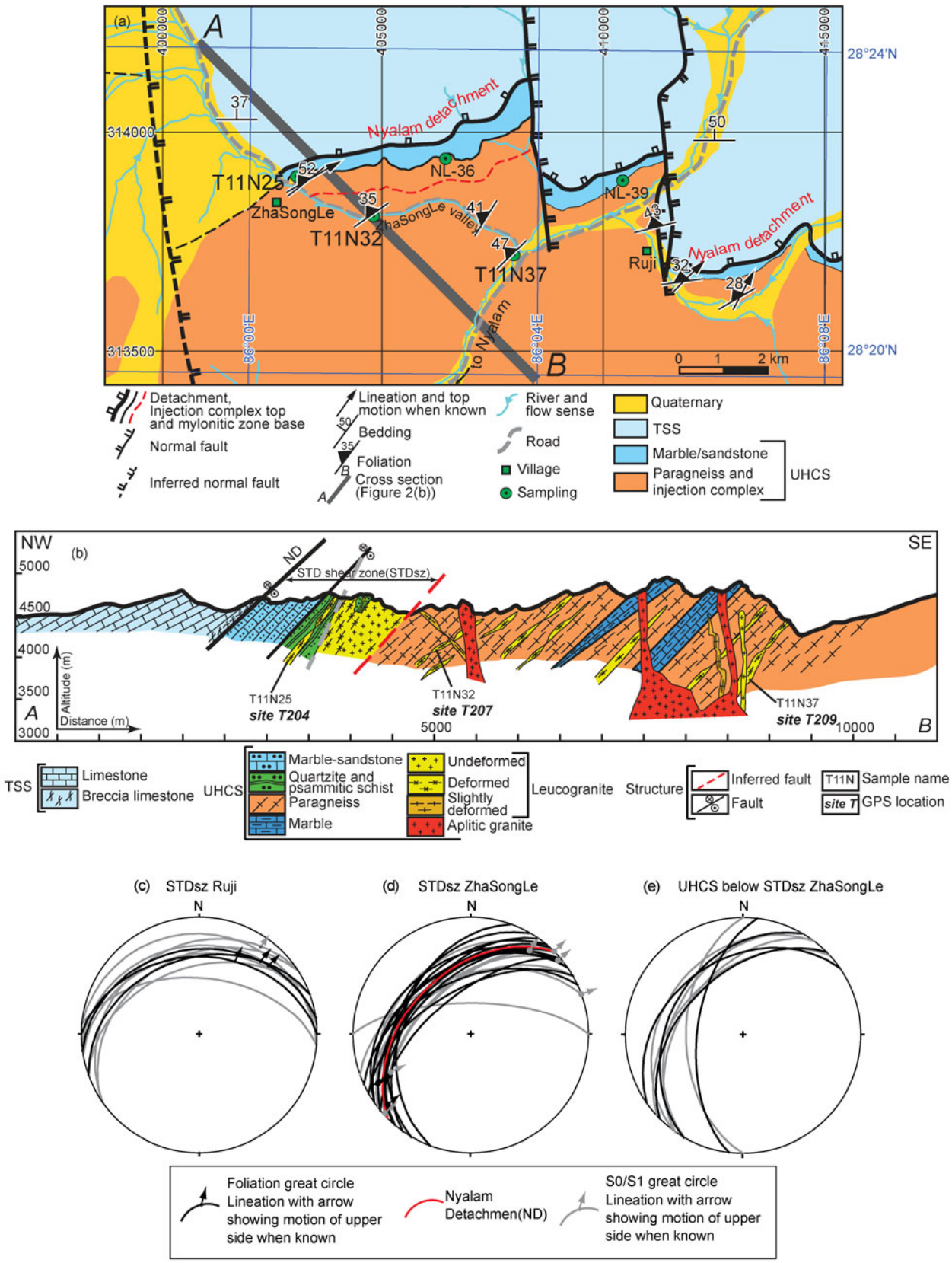

Figure 2 Structural map, cross section and foliation geometry in the UHCS north of Nyalam. (a) Structural map of Nyalam Detachment and its surrounding area (drawn from field observation, Landsat TM interpretation, Burchfiel et al. [26] and Zhu et al. [34]). The bold grey line corresponds to (b). Coordinates are UTM 45. (b) Cross section along ZhaSongLe valley (drawn from field observation). (c) to (e) are lower hemisphere Schmidt projection of structures in the UHCS. (c) STDsz in Ruji. (d) STDsz in ZhaSongLe. (e) UHCS below the STDsz, note the absence of stretching lineation.

by the late normal faults. The strong dip of the series gives access along the ZhaSongLe valley to a >3.5 km thick continuous section of the STDsz and UHCS (Figure 2(b)) that is not visible in most other locations.

Below the unmetamorphosed Ordovician limestone of the TSS, the ND corresponds to a ~10 m thick level of brecciated limestone lying above the STDsz. The STDsz is ~300 m thick and affects orange- weathering dolomites or marbles, green quartzite and dark psamitic schists and leucogranites. Within that shear zone, foliation trends ~N50°, dips ~52° to the North, and lineation strikes ~N55° (Figure 2(d)). Widely developed asymmetry fold and sigma-type porphyroclasts indicate an apparent dextral shear sense (Figure 3(a) and (b)) that would corresponds to a top to the North shear sense prior to tilting. Below the STDsz, foliation in the UHCS is almost parallel to that in the STDsz (Figure 2(e)), but there is no stretching lineation, nor any evidence for simple shear deformation. The UHCS series are mostly composed of gneiss with some marble layers [34]. Numerous leucocratic levels are strongly flattened parallel to the main shistosity while some undeformed dykes and granites crosscut that foliation (Figure 2(b)).

1.3 Existing geochronologic constraints

The only available U/Pb age in the UHCS along the Nyalam section is the 16.8±0.6 Ma $^{207}Pb/^{235}U$ age of monazite from a migmatite-granite [37]. Such age suggests a major melting event at that time that could be the source for the leucocratic dykes. However, the approximate location and the lack of description of the structural context preclude any other conclusion. Biotite and muscovite $^{40}Ar/^{39}Ar$ data, as well as zircon and apatite fission track ones, from samples located immediately below the STD suggest a two stages cooling history characterized by a fast cooling (⩾140°C/Ma) from ~16 Ma until 14 to 13 Ma, followed by a much slower cooling phase (⩽10°C/Ma) [21]. We interpret this brutal decrease in cooling rate as related to the end of motion, and hence exhumation and footwall cooling, on the ND at ~13 Ma. Such timing is compatible with the zircon fission track age pattern in the UHCS that suggests rapid cooling until prior to ~12.6 Ma, followed by slow cooling until at least ~7.4 Ma [38].

1.4 Structural relationships between leucogranites emplacement and deformation. A way to date UHCS deformation?

Along the ZhaSongLe valley, most leucocratic levels within the UHCS are almost parallel to the main shistosity. Most of these levels are strongly stretched and boudinated in the shistosity plane (Figure 3(c)–(f)) suggesting that the parallelism results mostly from deformation. In the STDsz that deformation appears close to simple shear, while it is close to pure shear below the shear zone. Below the STDsz some dykes are only slightly deformed (Figure 3(c)) or even undeformed (Figure 3(e)) and clearly crosscut the main foliation (Figure 2(b)). Samples of the stretched leucocratic levels have been sampled at three locations below the ND (Figure 2(b)).

Sample T11N25 was sampled at site T204, ~150 m below the ND within the STDsz. This leucocratic level containing quartz + k-feldspar + plagioclase + biotite + muscovite ± tourmaline ± Garnet is parallel to the surrounding schistosity within the psamitic shists. The schists show a clear stretching lineation and several top to the north shear criteria. The analysis of the corresponding thin section shows plagioclase (Pl) undulose extinction and quartz (Qtz) subgrain rotation recrystallization (SGR) (Figure 3(g)). This indicates that the deformation temperature is no lower than 400–500°C [39,40].

Sample T11N32 comes from a stretched leucocratic level (Figure 3(c)) containing quartz + k-feldspar + plagioclase + biotite + muscovite, which was sampled at site T207, ~1400 m structurally below the ND, parallel to the surrounding schistosity within the gneiss. The gneiss does not show any stretching lineation or any evidence for non-coaxial deformation. At this location the stretched dykes similar to T11N32 crosscut thinner folded and stretched leucocratic levels (Figure 3(d)) that thus appear to have been deformed prior to intrusion of the main leucocratic levels. The leucocratic levels incorporate schistose levels (Figure 3(d)), again suggesting intrusion after the onset of deformation. Analysis of T11N32 thin section shows that only small plagioclase or orthoclase grains show undulose extinction, but the larger ones remain rigid or show some microfractures, indicating that deformation probably initiated at temperature above 450°C [40] but and pursued at lower temperature.

Sample T11N37 is a leucocratic level containing quartz + k-feldspar + plagioclase + biotite + muscovite ± tourmaline, which was sampled at site T209, ~3500 m structurally beneath the ND. The level is stretched (Figure 3(e)) and presents lobed boundaries that appear to crosscut the surrounding foliation (Figure 3(f)) possibly indicating intrusion after the onset of deformation. The surrounding gneiss does not show any stretching lineation or any evidence for non-coaxial deformation.

The simplest interpretation of the observations above are: (1) the ⩾300 m thick dextral shear zone observed near ZhaSongLe corresponds to the STDsz tilted by later faults; (2) deformation linked with the STD affected a ⩾3500 m thick section of the UHCS; (3) below the shear zone deformation within the UHCS corresponds to pure shear; (4) leucocratic levels concordant to the foliation ubiquitous in the UHCS are probably syntectonic to the deformation and their emplacement age should lead a minimum age for the onset of that deformation; (5) some late leucocratic dykes crosscut the foliation below the STDsz, sealing the deformation.

2 Analytical method

To constrain the timing of emplacement of leucogranite sills,

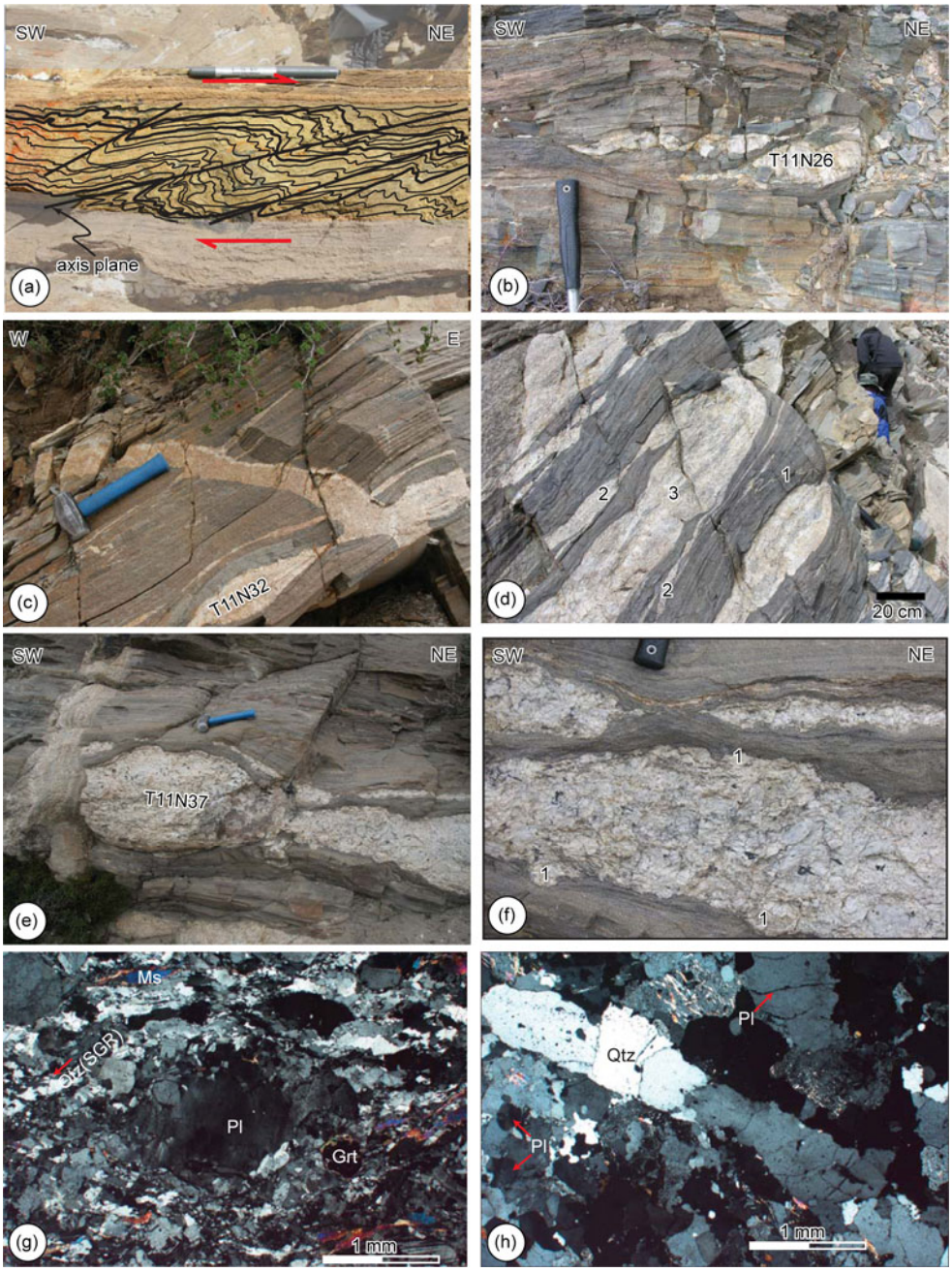

Figure 3 Typical geological features along ZhaSongLe valley. (a) Asymmetric fold of mylonitic dolomite in the STDsz, red arrows indicate the NE shear sense. (b) Stretched quartz level within the psamitic schists showing right-lateral shear (sample T11N26 GPS T204). (c) Stretched leucocratic level with weak internal foliation (sample T11N32) crosscut by a weakly deformed dyke (GPS T207 in Figure 2(b)). (d) Stretched leucocratic levels at site T207. Note the folded (1) and stretched (2) thin leucocratic levels crosscut by a less deformed leucogranite that incorporates schist levels (3). (e) Stretched leucocratic level (sample T11N37) crosscut by an undeformed dyke (GPS T209 in Figure 2(b)). (f) Detail of T11N37 leucocratic level. Note location where the leucoratic melt appears to intrude the foliation (1). (g) Polarized photomicrograph of sample T11N25 within the STDsz, plagioclase (Pl) undulose extinction and quartz (Qtz) subgrain rotation recrystallization (SGR) indicate the deformation temperature is no lower than 400–500°C [39,40]. (h) Polarized photomicrograph of sample T11N32 below the STDsz, only small plagioclase or orthoclase grains show undulose extinction, but the larger ones remain rigid or show some microfracture, indicating the deformation temperature is no lower than 450–500°C [40].

monazites or zircons were extracted from three samples. The zircon and monazite mineral separation was performed at the Yuneng mineral separation service lab in Langfang (Hebei province, China). About 3 kg of each sample were broken into ~1 cm^3 size pieces, prior to be crushed in 20 cm diameter stainless steel mortar using a XZW100 Vibration mill prototype for 3–5 s. The 75 μm to 400 μm size fraction was washed with water prior to electromagnetic, heavy liquid and high-frequency dielectric separations. From the higher density and non-sulfide fraction of the sample,

high-quality zircon and monazite were handpicked under a binocular from the non-magnetic and the magnetic fraction respectively. Minerals larger than 75 μm were mounted in epoxy resin, then abraded to reveal their center part and polished down to 1/4 μm with diamond paste. The mounts were coated with carbon for about 30 min prior to Back-scattered Electrons (BSE) and Cathodo-luminescence (CL) analysis. BSE and CL images were performed at the Laboratoire magmas et volcans (Clermont-Ferrand, France).

U-Th/Pb isotopic data for the monazites and zircon were obtained by laser ablation inductively coupled plasma spectrometry (LA-ICPMS) at the Laboratoire magmas et volcans (Clermont-Ferrand, France). Spot diameters of 9 μm for monazites and 20 μm for zircon were used. Single analyses consisted of 30 s of background integration with laser off followed by 1 min integration with the laser firing and a 30 s delay to wash out the previous sample (approximately 10 s for 6 orders of magnitude) and prepare the next analysis. The concentrations in U-Th/Pb were calibrated relative to the certified contents of Moacyr monazite standard [41] and GJ-1 zircon standard [42]. At the beginning and at the end of every run, repeated analyses of Manangoutry monazite standard [43] or 91500 zircon standard [44], treated as unknowns, independently control the reproducibility and accuracy of the corrections. Calculated ratios were exported and Concordia ages and diagrams were generated using Isoplot/Ex v. 3.0 software package by Ludwig [45].

3 Results and analysis of Monazite-Zircon U-Th/Pb ages

For zircon, the analytical results of the sample T11N25 were projected on $^{207}Pb/^{206}Pb$ versus $^{238}U/^{206}Pb$ diagrams [46], where the analytical measurements plot along a mixing line between the common Pb composition at the upper intercept and the zircon age at the lower intercept. This method is commonly used to date Phanerozoic zircons using *in situ* methods [42,47]. The closure temperature of magmatic zircon is usually higher than 900°C [48,49], in any case higher than 750–800°C [50], while the peak metamorphism temperature in upper HCS in this area is 570–690°C (samples N10 and N12 of Hodges et al. [51]), suggesting that the zircon crystallization ages will be preserved.

For monazites, the analytical results of sample T11N32 and T11N37 are plotted in $^{206}Pb/^{238}U$ versus $^{208}Pb/^{232}Th$ diagrams. The error ellipses often display a sub-vertical and reversely discordant linear array in these diagrams. In recent mineral, this is generally related to excess ^{206}Pb, produced by excess ^{230}Th, resulting from radioactive disequilibria in the decay chain of ^{238}U [52,53]. $^{208}Pb/^{232}Th$ dating of young monazites using *in situ* techniques is a well established geochronological method [9,54] based on the high Th content in monazite crystals, producing a significant amount of the daughter isotope ^{208}Pb in a very short time. Another advantage is the lack of long-lived intermediate daughter in the ^{232}Th-^{208}Pb decay chain [55]. The closure temperature of monazite is estimated at 725±25°C [52,56], in excess of 750°C [57] or 900°C [58]. This suggests that crystallization ages will be preserved during metamorphism [59,60]. The magmatic temperatures for the Himalaya leucogranites are likely no higher than ~650–750°C [61–64], meaning that the closure temperature is well above the crystallization temperature with limited diffusion of Pb in monazite and/or zircon [48,65,66] except huge fluid interactions. Compared to zircons, monazites are much less prone than zircons to yield inherited ages [52,56,67]. Thus, if the BSE images in monazite have no growth zones, U-Th/Pb spot analysis will be taken in different monazite crystals to obtain the representative emplacement ages, while two or three spot analysis will be taken in the same monazite crystals when the BSE images show the monazite growth zone to obtain the possible different emplacement ages.

3.1 Sample T11N25 (GPS T204, within STDsz)

The zircon grains are euhedral to subhedral, long prismatic to round, 50–150 μm long, with aspect ratios commonly of 1.5. CL images reveal that most of the zircon grains from this sample are gray, and a few of them have white cores. Th and U concentrations range from 80 to 2141 ppm, and from 143 to 27200 ppm, respectively. Th/U ratios are variable from 0.03 to 2.8 (Table S1). Among the 10 spots, three yield higher Th/U ratio from 0.28 to 2.8 in the (grayish) white cores, and 7 yield lower Th/U ratio from 0.03 to 0.05 in the grayish (black) borders. Though these zircon grains from borders have relatively low Th/U ratios, the oscillatory growth zoning indicates that they are magmatic (CL image in Figure 4(b)). LA-ICPMS U-Pb analyses show that the zircons have the early inherited ages and late emplacement age (Figure 4(a) and (b)).

Three spots from inherited zircon cores have a big time span from 365 to 2470 Ma (Table S1 and Figure 4(a)). The grayish core yield $^{207}Pb/^{206}Pb$ age at ~2470 Ma (Figure 4(a)) in the Pb/U concordia diagram. Variable ages from the cores indicate that the crystals come from different protoliths or have undergone multiple magmatic and/or metamorphic events.

Six spots from zircon borders and 1 spot from the core yield $^{206}Pb/^{238}U$ apparent ages from 16.9±0.2 to 17.5±0.2 Ma (Table S1, Figure 4(b)). In the Tera-Wasserburg diagram, the lower intercept age from these spots is 17.1±0.2 Ma (MSWD=1.4) (Figure 4(b), Table 1). The age of ~17 Ma represents the timing of emplacement and crystallization of the granite sill.

3.2 Sample T11N32 (GPS T207, STDsz below)

Most of monazites are euhedral to subhedral, long prismatic to round, 60–150 μm long, with aspect ratios commonly of

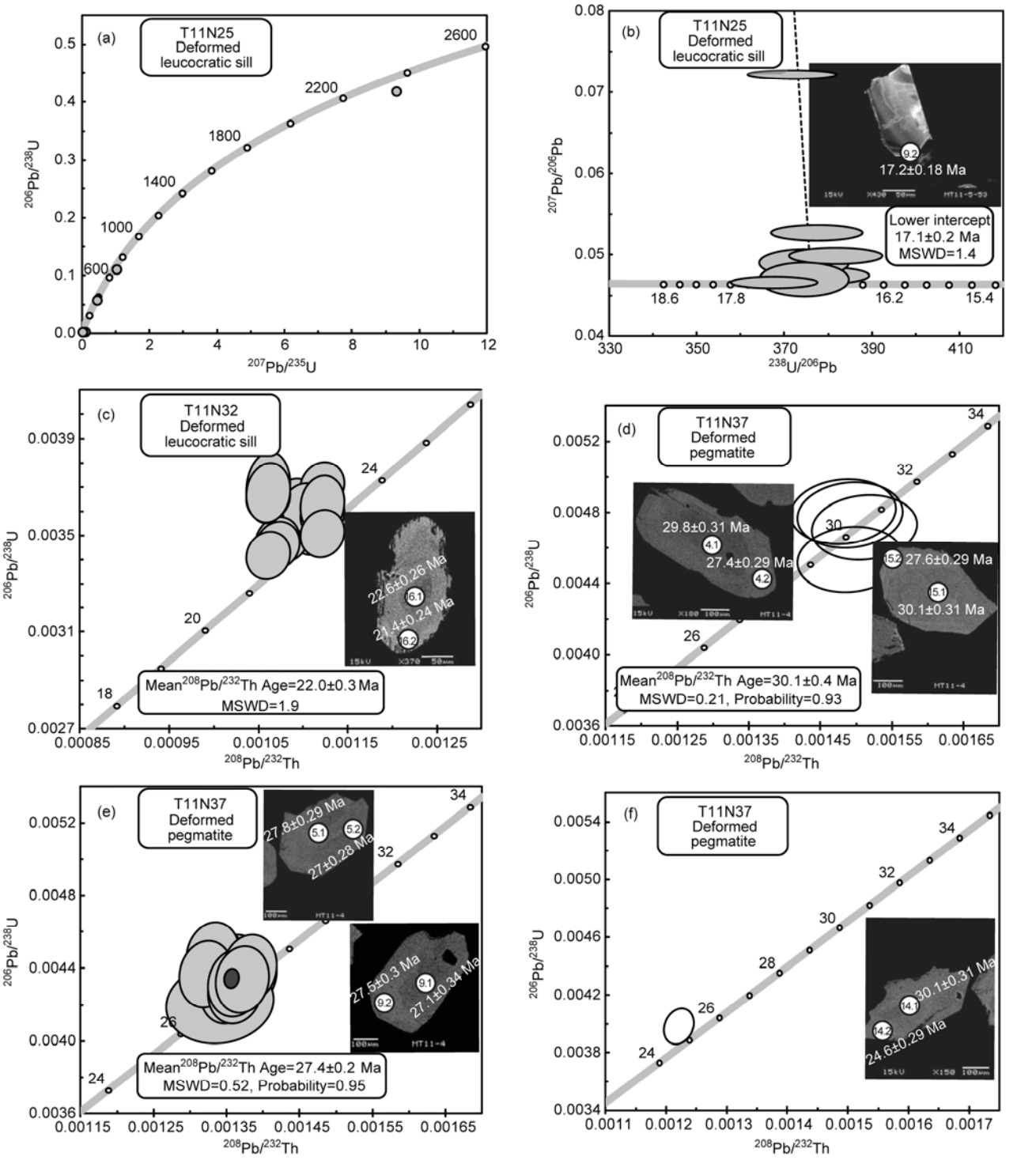

Figure 4 Zircon-monazite U-Th/Pb diagram, CL image for zircon and BSE images for monazites. The black circles filled with white colour in Back-scattered Electrons (BSE) and Cathodo-luminescence (CL) images represent the spot location of LA-ICPMS, the diameter of which is bigger than that of spot size because of the spot number filling in the circle. Detailed monazite U-Th/Pb results are in Tables S1–S3. (a) Zircon $^{206}Pb/^{238}U$-$^{207}Pb/^{235}U$ Concordia diagram for sample T11N25. (b) Zircon Tera-Wasserburg diagram for sample T11N25 and zircon CL image for border spot 9.2. (c) Monazite $^{206}Pb/^{238}U$- $^{206}Pb/^{232}Th$ diagram for sample T11N32 and BSE image for representative core and border yielding an almost homogeneous $^{206}Pb/^{232}Th$ age with a timing gap less than ~1.2 Ma. (d) Monazite $^{206}Pb/^{238}U$-$^{206}Pb/^{232}Th$ diagram for age population 1 of sample T11N37 and BSE images for representative cores and borders yielding a heterogeneous $^{206}Pb/^{232}Th$ age with a timing gap more than ~2.5 Ma, the cores and borders of which are located in age population 1 (d) and 2 (e), respectively. (e) Monazite $^{206}Pb/^{238}U$-$^{206}Pb/^{232}Th$ diagram for age population 2 of sample T11N37 and BSE images for representative cores and borders yielding an almost homogeneous $^{206}Pb/^{232}Th$ age with a timing gap less than ~0.8 Ma. (f) Monazite $^{206}Pb/^{238}U$-$^{206}Pb/^{232}Th$ diagram for age population 3 of sample T11N37 and BSE images for the border and core yielding a heterogeneous $^{206}Pb/^{232}Th$ age with a timing gap about ~5.5 Ma, the border and core of which is located in age population 3 (f) and 1 (d), respectively.

1.5. BSE images reveal that almost all the monazites have a homogeneous unzoned texture, indicating that most of the monazite ages will represent the youngest timing of emplacement and crystallization of the granite sill.

T11N32 shows a fairly homogeneous $^{208}Pb/^{232}Th$ age range from 21.4±0.2 to 22.6±0.3 Ma for 16 spots in 13 monazite grains (Table S2, Figure 4(c)) with one inherited grain at 411.2±4.0 Ma (spot 7 in Table S2). Three monazite grains with core-border texture yield the $^{208}Pb/^{232}Th$ core age from 21.4±0.3 to 22.6±0.3 Ma and border age from 21.4±0.3 to 21.6±0.2 Ma (Table S2, Figure 4(c)). The rest 10 monazite grains, including 2 borders and 8 cores, yield $^{208}Pb/^{232}Th$ age of 21.6–21.9 Ma and 21.5–22.6 Ma respectively (Table S2). All the 16 spots of 13 monazite grains, including 5 borders and 11 cores, yield a mean $^{208}Pb/^{232}Th$ age at 22.0±0.3 Ma(MSWD=1.9)(Table 1, Figure 4(c)). Sixteen monazites in sample T11N32 U-Th/Pb age described above span between ~21.4 and ~22.6 Ma confirming an early Miocene age of emplacement and crystallization of the deformed granite sill beneath the ND shear zone, with a mean $^{208}Pb/^{232}Th$ age at ~22 Ma.

3.3 Sample T11N37 (GPS T209, below the STDsz)

Most of monazites are euhedral, long prismatic, 200–300 μm long, with aspect ratios commonly of 1.5–2.5. BSE images reveal that many of monazites have a zoned texture, the cores of which usually display euhedral shapes indicating that the ages from cores can represent the timing of emplacement and crystallization of the granite sill [68]. LA-ICPMS U-Th/Pb analyses show that three age groups can be identified, which is population 1 with a mean $^{208}Pb/^{232}Th$ age at 30.1±0.4 Ma (Table 1, Figure 4(d)), population 2 with a mean $^{208}Pb/^{232}Th$ age at 27.4±0.2 Ma (Table 1, Figure 4(e)) and population 3 with a $^{208}Pb/^{232}Th$ age at 24.6±0.3 Ma (Table 1, Figure 4(f)), respectively.

In 5 monazite grains of sample T11N37, spots in cores shows a fairly homogeneous $^{208}Pb/^{232}Th$ age range from 30.4±0.3 to 29.8±0.3 Ma (Table S3, Figure 4(d)) yielding a mean $^{208}Pb/^{232}Th$ age at 30.1±0.4 Ma (MSWD=0.21) (Table 1, Figure 4(d)). The fairly homogeneous $^{208}Pb/^{232}Th$ age range indicates an early Oligocene crystallization at ~30 Ma. In the 5 monazite grains, 4 spots in borders show a $^{208}Pb/^{232}Th$ age range from 26.8±0.3 to 27.7±0.3 Ma (Table S3, Figure 4(e)). One spot in border of the grain 14 shows a $^{208}Pb/^{232}Th$ age at 24.6±0.3 Ma (Tables 1 and S3, Figure 4(f)), possibly linked with fluid circulation.

In 10 monazite grains of sample T11N37, 8 spots in the cores and 8 spots in the borders show a fairly homogeneous $^{208}Pb/^{232}Th$ age range from 27.8±0.3 to 26.9±0.3 Ma and 27.8±0.3 to 26.7±0.3 Ma (Table S3). Combining with the former 4 spots described above, the 20 spots, including 8 cores and 12 borders, yield a mean $^{208}Pb/^{232}Th$ age at 27.4±0.2 Ma(MSWD=1.9)(Table 1, Figure 4(e)). The fairly homogeneous $^{208}Pb/^{232}Th$ age range indicates a late Oligocene emplacement and crystallization at ~27.5 Ma.

4 Discussion

4.1 Timing of ductile deformation beneath the ND

Sample T11N25, the leucogranitic level strongly deformed in the STDsz (~150 m structurally below the ND), has an emplacement age of 17.1±0.2 Ma. This implies that ductile deformation in this location occurred at or some time after that date. The time lag between the emplacement and the

Table 1 Summary of zircon and monazite LA-ICPMS U-Th/Pb (this study) and mica and k-feldspar $^{40}Ar/^{39}Ar$ [21] data [a)]

Section	Number	Rock type	Mineral type	Method	Population	Age type	Age results	Spot locations/grain numbers; steps	Reference
STDsz	NL-39	Mylonite	Biotite	$^{40}Ar/^{39}Ar$		Weighted mean plateau	15.0±0.4	11s/12(2-12), 99.2% of gas	Wang et al. [21]
						Isochron age	15.0±0.7		
	NL-36	Mylonite	Muscovite	$^{40}Ar/^{39}Ar$		Preferred age, no plateau	15.6±0.7	5s/13(6-10), 76.15% of gas	
						Isochron age	14.9±1.9		
			Apatite	$^{40}Ar/^{39}Ar$		Fission track	11.9±2.1		
			K-feldspar	$^{40}Ar/^{39}Ar$		K-feldspar MDD	See Figure 7e[21]		
	T11N25	Deformed leucocratic sill	Zircon	LA-ICPMS		Lower intercept age	17.1±0.2	(6b+1c)/7g	This study
STDsz below	T11N32	Deformed leucocratic sill	Monazite	LA-ICPMS		Mean $^{208}Pb/^{232}Th$	22.0±0.3	3bc/3g and (2b+8c)/10g	This study
	T11N37	Deformed pegmatite	Monazite	LA-ICPMS	1	Mean $^{208}Pb/^{232}Th$	30.1±0.4	5c/5g	
					2	Mean $^{208}Pb/^{232}Th$	27.4±0.2	4b/4g and (2b+2c+6bc)/10g	
					3	Mean $^{208}Pb/^{232}Th$	24.6±0.3	1b/1g	

a) b, border of spot location; c, core of spot location; g, zircon or monazite grain; s, steps. Ma±2 σ for $^{208}Pb/^{232}Th$ and concordia age; Ma±1 σ for $^{40}Ar/^{39}Ar$ age.

deformation cannot be precisely known, but deformation occurred before the granite cooled below ~500°C. This temperature was reached at ~16 Ma according to the cooling history built from the data of Wang et al. [21] (Table 1, Figure 5), thus suggesting that deformation occurred immediately after, or possibly during, the granite emplacement. T11N25 emplacement age is similar within errors to the 16.8±0.8 Ma age of a Migmatite-granite sampled deeper in the UHCS [37]. This suggests that dykes found right beneath the STD originate much deeper in the UHCS. Dykes of similar ages are also found in other portion of the STDsz: ~16.5 Ma in the Qomolangma area (~87°E, C Figure 1) [11,15] and 16±0.5 Ma in Dinggye (~87.8°E, S Figure 1) [14]. In the Qomolongma area, at least two leucogranite generations have been distinguished: one mylonitic parallel to the Qomolangma detachement (QD, local name for the STDsz) foliation is crosscut by variably deformed dykes. All dykes yield essentially the same $^{208}Pb/^{232}Th$ ion probe monazite ages: 16.8±0.8 Ma for a crosscutting dyke, 16.4±0.6 Ma for a crosscutting but deflected dyke, and 16.2±0.8 Ma for a mylonitic dyke [15]. These authors thus proposed that the QD was active at ~17 Ma. The data also imply that deformation was over at that time below the STDsz. In Dinggye, dating of monazites and zircons in deformed and undeformed leucogranites suggests that ductile deformation lasted until at least 16 Ma but ended prior to 15 Ma in the STD shear zone ~100 m below the detachment [14]. There is a striking similarity among all these data that demonstrate that the STDsz was active at ~17 Ma at least from Nyalam to Dinggye. However, the timing of initiation of the STDsz is much more difficult to constrain.

In most cases, this age has been determined by assuming that leucogranite emplacement where linked with the STD motion either because they would result from exhumation induced by motion along the fault [31] or because they would have trigger the motion [26]. In the central Himalaya, most leucogranite emplacement ages are Early-Middle Miocene (~24 to ~12 Ma) [4,9,12,29,31,36,37,69]; but some leucosome yield Oligocene ages (33–23 Ma) [6,23].

Aproximately 80 km west of Nyalam, along the Gyirong section(G, Figure 1), Yang et al. [24] describe a mylonitic leucogranite deformed in the STDsz. Two samples (TG01 and TG11, respectively ~1.4 and ~1.8 km below the top of the STDsz) from this granite yield similar concordant SHRIMP U/Pb zircon age population: inherited cores older than 500 Ma and rims spanning in age from ~38 to ~19 Ma with most of the ages at 25–27.5 Ma. Both samples also show some young ages at ~19–23 Ma (21.8±1.3 Ma on average). As they interpret this granite as syntectonic, Yang et al. [24] conclude that the STDsz was active at ~26 Ma and possibly since ~36 Ma.

Along the Nyalam section, sample T11N32, ~1400 m structurally below the ND, emplaced at 22.0±0.3 Ma. This sill being most probably syntectonic, this constrains the deformation to have been active at ~22 Ma at that depth.

Sample T11N37 emplaced at 27.4±0.2 Ma suggesting that deformation was active at that time ~3500 m below the ND. In fact the age pattern observed for T11N37 monazites with four core ages yielding an average age of 30.1±0.4 Ma, 16 cores and rim ages with a mean age of 27.4±0.2 Ma and one rim at 24.6±0.3 Ma is comparable to the age pattern observed in zircons of samples TG01 and TG11 of Yang

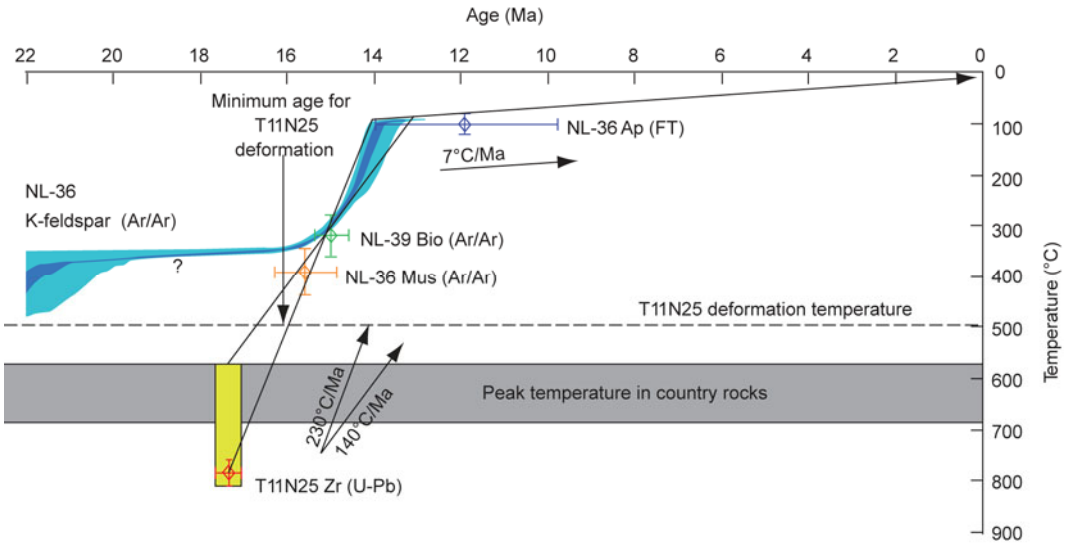

Figure 5 Cooling history of the Nyalam detachment footwall. Cooling history built from NL-36 and NL-39 $^{40}Ar/^{39}Ar$ and apatite Fission track data of Wang et al. [21] and T11N25 zircon (this study). The high temperature history deduced from the k-feldspar is barely compatible with T11N25 zircon and NL-36 muscovite ages, and is thus figured with a question mark. The exact temperature at the time of T11N25 emplacement is unknown, but is above 500°C (deformation temperature of T11N25), and probably at 570–690°C (peak metamorphism) [51]. In any case a rapid cooling phase (⩾140°C/Ma) starts at ~17.5 Ma and lasts until 14–13 Ma.

et al. [24]. In both cases the precise interpretation of the ages is complicated by the existence of three populations. Our preferred interpretation is that the oldest population corresponds to first zircon/monazite crystallisations at the time of melting while the most important population corresponds to a second crystallization event at the time of crystallization, the few younger ages would correspond to limited late recrystallization possibly linked with fluid circulation. If this interpretation is correct, the ages we and Yang et al. [24] propose for deformation linked in the STDsz will be validated, but there is no proof that the deformation started at the time of the first crystallisation event (~30 and ~36 Ma respectively).

About 100 km east of Nyalam, monazites and zircons have been dated in gneiss, deformed leucogranites and undeformed leucogranites in the Kangshung valley near the Qomolongma ~3500 m structurally below the QD [4]. The ages of deformed and undeformed leucrogranites suggest that deformation ended between 20.9±0.4 and 16.7±0.4 Ma at this location.

In summary there are good evidences that the STDsz was active at ~17 Ma from Nyalam to Dinggye. At these locations deformation linked with the STD stopped at ~12 Ma [14]. In the UHCS rocks below the STDsz deformation seems to be closer to pure shear than to simple shear, which is also found in the other portion of the STD [35,70] and probably started prior to 22.0±0.3 Ma and 27.4±0.2, 1500 and 3500 m below the STD respectively. In Gyirong deformation in the STDsz was active at ~26 Ma if the leucogranite is effectively syntectonic. An earlier deformation episode (at ~36 Ma in Gyirong and ~30 Ma in Nyalam) stays speculative as the syntectonic nature of the early fusion events cannot be proved.

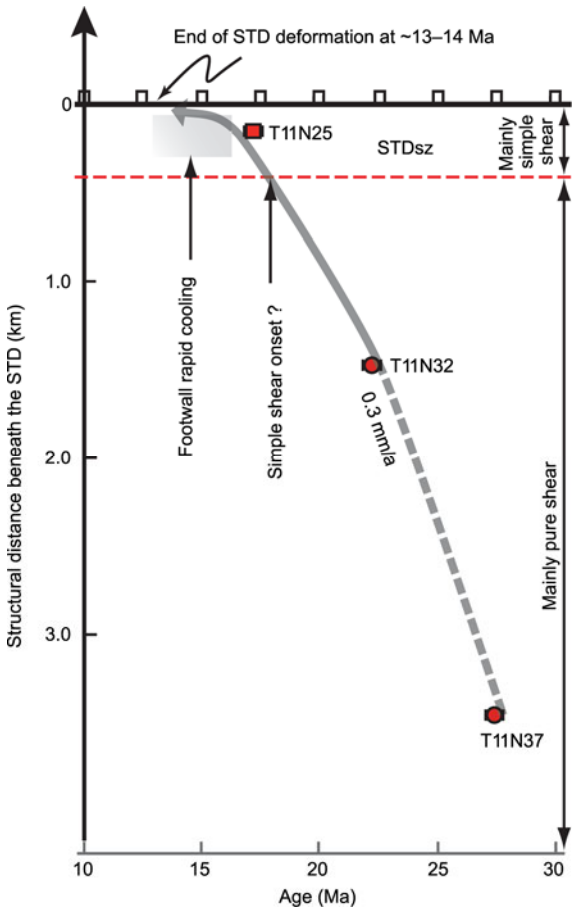

Figure 6 Diachronism of the ductile deformation beneath the Nyalam Detachment. Dykes emplacement ages (*x* axis) plotted as a function of the distance beneath the STD (*y* axis). Red square and circles correspond to zircon and monazite ages, respectively. As T11N32 and T11N37 are interpreted as syntectonic, and the minimum age of deformation for T11N25 is ~16 Ma (Figure 5), the grey arrow describes the apparent migration of the ductile deformation age. Footwall rapid cooling is taken from Wang et al. [21] with an age range between ~16 and ~13 Ma (Figure 5).

4.2 Migration of ductile deformation beneath the ND. A new model for STDsz initiation?

The timing of the end of deformation in the STDsz and on the STD can be constrained from crosscutting relationships and footwall cooling histories [14]. In contrast the timing of the onset of deformation is much more difficult to constrain. In this contribution we suggest that deformation linked with the STD in the UHCS below the STDsz initiated prior to ~27.4 Ma by directly dating deformed leucogranites that we interpret as syntectonic (see above).

When the ages of possibly syntectonic dykes are plotted with respect to their depth (Figure 6) a striking relationship appears: deformation gets younger upwards. If this assertion is correct it would confirm the proposition of upward progressive deformation localization proposed by Leloup et al. [14] in the Dinggye region and of Cottle et al. [25] for the Dzakaa Chu valley. Studies from other detachment zones also suggest an upward migration of ductile deformation from the detachment footwall to its surface [71–74].

From these data we can propose a new model for deformation migration below the ND. Deformation would have started by pure shear deformation with an almost vertical shortening below the STDsz. Such deformation would then have migrated upwards at a rate of ~0.3 mm/a. At ~18 Ma simple shear deformation would have initiated in what is now the STDsz (Figure 6). This scenario is in good agreement with preliminary data that suggest that the end of deformation within the UHCS also migrated upward trough time [75]. The model would need further data to be confirmed but would have important implications on Himalayan tectonics. (1) Deformation that related with nearly vertical shortening would have started prior to ~27.5 Ma and would have migrated upwards. (2) STDsz with significant top to the north motion would have initiated only at ~18 Ma, and thus would have lasted less than ~5 Ma. (3) Such timing is barely compatible with the lower channel flow hypothesis.

Our model is however apparently not consistent with the data of Yang et al. [24] that propose syntectonic magmatism

in the STDsz at ~27 Ma or even possibly ~36 Ma. This could be due either to the fact that the leucogranite near Gyirong are in fact not syntectonic or to differences in age between different sections of the STDsz.

5 Conclusion

We propose a new conceptual model of deformation migration through the UHCS based on observations within and below the Nyalam shear zone. In this model, deformation starts prior to ~27.5 Ma with vertical flattening at depth. This deformation progressively migrates upwards at a rate of ~0.3 mm/a. At ~18 Ma deformation switches to top to the North simple shear within the STDsz. In the Nyalam shear zone, such ductile deformation lasts until ~15 Ma while brittle motion on the detachement continues until 14–13 Ma. Much more field and geochronology data with a careful observation of the structural relationships between dyke emplacement and deformation, and a careful discussion on the U-Th/Pb ages, would be necessary to validate, or disclaim, this model. If confirmed, the model would have major implications on the timing and amount of motion of the STDsz in particular and on the genesis of low angle detachments in general.

This work was supported by Synthetic Investigation on the Environment in Polar Region (*CHINARE2012-02-02*) *and the SYSTER Program of the French INSU-CNRS.*

1 Burg J P, Brunel M, Gapais D, et al. Deformation of leucogranites of the crystalline Main Central Sheet in Southern Tibet (China). J Struct Geol, 1984, 6: 535–542
2 Brown R L, Nazarchuk J H. Annapurna Detachment Fault in the Greater Himalaya of Central Nepal. Geol Soc Lond spec publ, 1993, 74: 461–473
3 Cottle J M, Jessup M J, Newell D L, et al. Structural insights into the early stages of exhumation along an orogen-scale detachment: The South Tibetan Detachment System, Dzakaa Chu section, eastern Himalaya. J Struct Geol, 2007, 29: 1781–1797
4 Cottle J M, Searle M P, Horstwood M S A, et al. Timing of midcrustal metamorphism, melting, and deformation in the mount Everest region of Southern Tibet revealed by U(-Th)-Pb geochronology. J Geol, 2009, 117: 643–664
5 Godin L, Brown R L, Hanmer S, et al. Back folds in the core of the Himalayan orogen: An alternative interpretation. Geology, 1999, 27: 151–154
6 Godin L, Parrish R R, Brown R L, et al. Crustal thickening leading to exhumation of the Himalayan metamorphic core of central Nepal: Insight from U-Pb Geochronology and $^{40}Ar/^{39}Ar$ Thermochronology. Tectonics, 2001, 20: 729–747
7 Guillot S, Hodges K, Lefort P, et al. New constraints on the age of the Manaslu leucogranite: Evidence for episodic tectonic denudation in the central Himalayas. Geology, 1994, 22: 559–562
8 Harrison T M, Grove M, McKeegan K D, et al. Origin and episodic emplacement of the Manaslu intrusive complex, central Himalaya. J Petrol, 1999, 40: 3–19
9 Harrison T M, Mckeegan K D, Lefort P. Detection of inherited monazite in the Manaslu leucogranite by $^{208}Pb/^{232}Th$ ion microprobe dating-crystallization age and tectonic implications. Earth Planet Sci Lett, 1995, 133: 271–282
10 Harrison T M, Ryerson F J, LeFort P, et al. A late Miocene-Pliocene origin for the Central Himalayan inverted metamorphism. Earth Planet Sci Lett, 1997, 146: E1–E7
11 Hodges K, Bowring S, Davidek K, et al. Evidence for rapid displacement on Himalayan normal faults and the importance of tectonic denudation in the evolution of mountain ranges. Geology, 1998, 26: 483–486
12 Hodges K V, Parrish R R, Searle M P. Tectonic evolution of the central Annapurna Range, Nepalese Himalayas. Tectonics, 1996, 15: 1264–1291
13 Kali E, Leloup P H, Arnaud N, et al. Exhumation history of the deepest central Himalayan rocks, Ama Drime range: Key pressure-temperature-deformation-time constraints on orogenic models. Tectonics, 2010, 29: 1–31
14 Leloup P H, Maheo G, Arnaud N, et al. The South Tibet Detachment shear zone in the Dinggye area Time constraints on extrusion models of the Himalayas. Earth Planet Sci Lett, 2010, 292: 1–16
15 Murphy M A, Harrison T M. Relationship between leucogranites and the Qomolangma Detachment in the Rongbuk Valley, south Tibet. Geology, 1999, 27: 831–834
16 Noble S R, Searle M P. Age of crustal melting and leucogranite formation from U-Pb zircon and monazite dating in the western Himalaya, Zanskar, India. Geology, 1995, 23: 1135–1138
17 Sakai H, Sawada M, Takigami Y, et al. Geology of the summit limestone of Mount Qomolangma (Everest) and cooling history of the Yellow Band under the Qomolangma Detachment. Isl Arc, 2005, 14: 297–310
18 Searle M P, Godin L. The South Tibetan Detachment and the Manaslu leucogranite: A structural reinterpretation and restoration of the Annapurna-Manaslu Himalaya, Nepal. J Geol, 2003, 111: 505–523
19 Searle M P, Parrish R R, Hodges K V, et al. Shisha Pangma leucogranite, south Tibetan Himalaya: Field relations, geochemistry, age, origin, and emplacement. J Geol, 1997, 105: 295–317
20 Streule M J, Searle M P, Waters D J, et al. Metamorphism, melting, and channel flow in the Greater Himalayan Sequence and Makalu leucogranite: Constraints from thermobarometry, metamorphic modeling, and U-Pb geochronology. Tectonics, 2010, 29: TC5011
21 Wang Y, Li Q, Qu G S. $^{40}Ar/^{39}Ar$ thermochronological constraints on the cooling and exhumation history of the South Tibetan Detachment System, Nyalam area, southern Tibet. In: Law R D, Searle M P, Godin L, eds. Channel Flow, Ductile Extrusion and Exhumation in Continental Collision Zones. Geol Soc Lond spec publ, 2006, 268: 327–354
22 Yu J J, Zeng L S, Liu J, et al. Early Miocene leucogranites in Dinggye area, southern Tibet: Formation mechanism and tectonic implications (in Chinese). Acta Petrol Sin, 2011, 27: 1961–1972
23 Coleman M E. U-Pb constraints on oligocene-miocene deformation and anatexis within the central Himalaya, Marsyandi valley, Nepal. Am J Sci, 1998, 298: 553–571
24 Yang X Y, Zhang J J, Qi G W, et al. Structure and deformation around the Gyirong basin, north Himalaya, and onset of the South Tibetan Detachment System. Sci China Earth Sci, 2009, 52: 1046–1058
25 Cottle J M, Waters D J, Riley D, et al. Metamorphic history of the South Tibetan Detachment System, Mt. Everest region, revealed by RSCM thermometry and phase equilibria modelling. J Metamorph Geol, 2011, 29: 561–582
26 Burchfiel B C, Chen Z, Hodges K V, et al. Detachment System, Himalayan orogen: Extension contemporaneous with and parallel to shortening in a collisional mountain belt. Geo Soc Am spec publ, 1992, 269: 1–41
27 Burg J P. Carte Géologique du Sud Tibet. In: Mo Geology/CNRS, ed, Ministry of Geology/CNRS, Beijing/Paris, 1983
28 Carosi R, Lombardo B, Molli G, et al. The South Tibetan Detachment System in the Rongbuk valley, Everest region. Deformation features and geological implications. J Asian Earth Sci, 1998, 16: 299–311
29 Edwards M A, Kidd W S F, Li J X, et al. Multi-stage development of

the Southern Tibet Detachment System near Khula Kangri. New data from Gonto La. Tectonophysics, 1996, 260: 1–19
30 Zhang J J, Santosh M, Wang X X, et al. Tectonics of the northern Himalaya since the India-Asia collision. Gondwana Res, 2012, 21: 939–960
31 Harris N B W, Caddick M, Kosler J, et al. The pressure-temperature-time path of migmatites from the Sikkim Himalaya. J Metamorph Geol, 2004, 22: 249–264
32 Godin L, Grujic D, Law R D, et al. Channel flow, ductile extrusion and exhumation in continental collision zones: An introduction. In: Law R D, Searle M P, Godin L, eds. Channel Flow, Ductile Extrusion and Exhumation in Continental Collision Zones. Geol Soc Lond spec publ, 2006, 268: 1–23
33 Yin A. Cenozoic tectonic evolution of the Himalayan orogen as constrained by along-strike variation of structural geometry, exhumation history, and foreland sedimentation. Earth-Sci Rev, 2006, 76: 1–131
34 Zhu T X, Zou G F, Li J Z, et al. Report of Regional Geological Survey of Nielam County (1/250 000) (in Chinese). Beijing: Geological Publishing House, 2002. 1–363
35 Law R D, Jessup M J, Searle M P, et al. Telescoping of isotherms beneath the South Tibetan Detachment System, Mount Everest Massif. J Struct Geol, 2011, 33: 1569–1594
36 Wu C D, Nelson K D, Wortman G, et al. Yadong cross structure and South Tibetan Detachment in the east central Himalaya (89°–90°E). Tectonics, 1998, 17: 28–45
37 Schärer U, Xu R H, Allegre C J. U-(Th)-Pb systematics and ages of Himalayan leucogranites, South Tibet. Earth Planet Sci Lett, 1986, 77: 35–48
38 Wang A, Garver J I, Wang G C, et al. Episodic exhumation of the Greater Himalayan Sequence since the Miocene constrained by fission track thermochronology in Nyalam, central Himalaya. Tectonophysics, 2010, 495: 315–323
39 Stipp M, Stunitz H, Heilbronner R, et al. The eastern Tonale fault zone: A "natural laboratory" for crystal plastic deformation of quartz over a temperature range from 250 to 700 degrees C. J Struct Geol, 2002, 24: 1861–1884
40 Tullis J A, Yund R A. The brittle-ductile transition in feldspar aggregates: An experimental study. In: Evans B, Wong T F, eds. Fault Mechanics and Transport Properties of Rocks. London: Academic Press, 1992. 89–117
41 Seydoux-Guillaume A M, Wirth R, Deutsch A, et al. Microstructure of 24–1928 Ma concordant monazites: Implications for geochronology and nuclear waste deposits. Geochim Cosmochim Acta, 2004, 68: 2517–2527
42 Jackson S E, Pearson N J, Griffin W L, et al. The application of laser ablation-inductively coupled plasma-mass spectrometry to *in situ* U-Pb zircon geochronology. Chem Geol, 2004, 211: 47–69
43 Paquette J L, Tiepolo M. High resolution (5 μm) U-Th-Pb isotope dating of monazite with excimer laser ablation (ELA)-ICPMS. Chem Geol, 2007, 240: 222–237
44 Wiedenbeck M, Alle P, Corfu F, et al. Three natural zircon standards for U-Th-Pb, Lu-Hf, trace-element and REE analyses. Geostand Newslett, 1995, 19: 1–23
45 Ludwig K R. Isoplot 3.00 a geochronological toolkit for Microsoft Excel. Berkley Geoch Cent Spec Pub, 2003. 4
46 Tera F, Wasserburg G J. U-Th-Pb systematics in 3 Apollo 14 basalts and problem of initial Pb in Lunar rocks. Earth Planet Sci Lett, 1972, 14: 281–304
47 Claoué-Long J, Compston W, Roberts J, et al. Two carboniferous ages: A comparison of SHRIMP zircon dating with conventional zircon ages and $^{40}Ar/^{39}Ar$ analysis. In: Berggren W A, Kent D V, Aubry M P, et al, eds. Geochronology, Time Scales & Stratigraphic Correlation. SEPM Spec Publ, 1995, 54: 1–22
48 Cherniak D J, Watson E B. Pb diffusion in zircon. Chem Geol, 2001, 172: 5–24
49 Lee J K W, Williams I S, Ellis D J. Pb, U and Th diffusion in natural zircon. Nature, 1997, 390: 159–162
50 Clemens J D. S-type granitic magmas-petrogenetic issues, models and evidence. Earth-Sci Rev, 2003, 61: 1–18
51 Hodges K V, Burchfiel B C, Royden L H, et al. The metamorphic signature of contemporaneous extension and shortening in the Central Himalayan Orogen-data from the Nyalam Transect, Southern Tibet. J Metamorph Geol, 1993, 11: 721–737
52 Parrish R R. U-Pb dating of monazite and its application to geological problems. Can J Earth Sci, 1990, 27: 1431–1450
53 Schärer U. The effect of initial ^{230}Th disequilibrium on young U-Pb ages: The Makalu case, Himalaya. Earth Planet Sci Lett, 1984, 67: 191–204
54 Stern R A, Sanborn N. Monazite U-Pb and Th-Ph geochronology by high-resolution secondary ion mass spectrometry. In: Radiogenic Age and Isotopic Studies. Curr Res Geol Surv Canada, Ottawa, 1998, 11: 1–18
55 Getty S R, Depaolo D J. Quaternary geochronology using the U-Th-Pb method. Geochim Cosmochim Acta, 1995, 59: 3267–3272
56 Copeland P, Parrish R R, Harrison T M. Identification of inherited radiogenic Pb in monazite and its implications for U-Pb systematics. Nature, 1988, 333: 760–763
57 Spear F S, Parrish R R. Petrology and cooling rates of the Valhalla complex, British Columbia, Canada. J Petrol, 1996, 37: 733–765
58 Braun I, Montel J M, Nicollet C. Electron microprobe dating of monazites from high-grade gneisses and pegmatites of the Kerala Khondalite Belt, southern India. Chem Geol, 1998, 146: 65–85
59 Cocherie A, Mezeme E B, Legendre O, et al. Electron-microprobe dating as a tool for determining the closure of Th-U-Pb systems in migmatitic monazites. Am Mineral, 2005, 90: 607–618
60 Foster G, Gibson H D, Parrish R, et al. Textural, chemical and isotopic insights into the nature and behaviour of metamorphic monazite. Chem Geol, 2002, 191: 183–207
61 Clemens J D, Vielzeuf D. Constraints on melting and magma production in the crust. Earth Planet Sci Lett, 1987, 86: 287–306
62 Montel J M. A model for monazite/melt equilibrium and application to the generation of granitic magmas. Chem Geol, 1993, 110: 127–146
63 Scaillet B, Pichavant M, Roux J. Experimental crystallization of leucogranite magmas. J Petrol, 1995, 36: 663–705
64 Searle M P. Emplacement of Himalayan leucogranites by magma injection along giant sill complexes: Examples from the Cho Oyu, Gyachung Kang and Everest leucogranites (Nepal Himalaya). J Asian Earth Sci, 2000, 17: 773–783
65 Smith H A, Giletti B J. Lead diffusion in monazite. Geochim Cosmochim Acta, 1997, 61: 1047–1055
66 Viskupic K, Hodges K V, Bowring S A. Timescales of melt generation and the thermal evolution of the Himalayan metamorphic core, Everest region, eastern Nepal. Contrib Mineral Petrol, 2005, 149: 1–21
67 Kelsey D E, Clark C, Hand M. Thermobarometric modelling of zircon and monazite growth in melt-bearing systems: Examples using model metapelitic and metapsammitic granulites. J Metamorph Geol, 2008, 26: 199–212
68 Orejana D, Merino E, Villaseca C, et al. Electron microprobe monazite geochronology of granitic intrusions from the Montes de Toledo batholith (central Spain). Geol J, 2012, 47: 41–58
69 Daniel C G, Hollister L S, Parrish R R, et al. Exhumation of the Main Central Thrust from lower crustal depths, eastern Bhutan Himalaya. J Metamorph Geol, 2003, 21: 317–334
70 Law R D, Searle M P, Simpson R L. Strain, deformation temperatures and vorticity of flow at the top of the Greater Himalayan Slab, Everest Massif, Tibet. J Geol Soc Lond, 2004, 161: 305–320
71 Agard P, Augier R, Monie P. Shear band formation and strain localization on a regional scale: Evidence from anisotropic rocks below a major detachment (Betic Cordilleras, Spain). J Struct Geol, 2011, 33: 114–131
72 Behr W M, Platt J P. A naturally constrained stress profile through the middle crust in an extensional terrane. Earth Planet Sci Lett, 2011, 303: 181–192
73 Cooper F J, Platt J P, Platzman E S, et al. Opposing shear senses in a

subdetachment mylonite zone: Implications for core complex mechanics. Tectonics, 2010, 29: 1–18
74 Davis G A. Rapid upward transport of mid-crustal mylonitic gneisses in the footwall of a Miocene Detachment Fault, Whipple Mountains, Southeastern California. Geol Rundsch, 1988, 77: 191–209
75 Leloup P H, Liu X B, Mahéo G, et al. Quantification of progressive deformation localization below the STD shear zone (Himalaya). Geophys Res Abstract, 2012, 14: EGU2012–10235

Supporting Information

Table S1 Zircon LA-ICPMS U-Pb data of sample T11N25
Table S2 Monazite LA-ICPMS U-Th/Pb data of sample T11N32
Table S3 Monazite LA-ICPMS U-Th/Pb data of sample T11N37

The supporting information is available online at csb.scichina.com and www.springerlink.com. The supporting materials are published as submitted, without typesetting or editing. The responsibility for scientific accuracy and content remains entirely with the authors.